AGU PUBLICATIONS

JGR

Journal of Geophysical Research: Solid Earth

RESEARCH ARTICLE
10.1002/2016JB013883

Key Points:
- Combined tsunami and land-based geodetic inversions can offer improved seismogenic fault resolution for tsunamigenic megathrust earthquakes
- The 2015 Illapel earthquake excited tsunami waves observed across Pacific-South America, with transoceanic records as far as Kuril Islands
- Inverse model shows that most slip in 2015 Illapel earthquake occurs just offshore, with little near-trench contribution required

Supporting Information:
- Supporting Information S1
- Table S1

Correspondence to:
A. Williamson,
amy.williamson@gatech.edu

Citation:
Williamson, A., A. Newman, and P. Cummins (2017), Reconstruction of coseismic slip from the 2015 Illapel earthquake using combined geodetic and tsunami waveform data, *J. Geophys. Res. Solid Earth*, *122*, 2119–2130, doi:10.1002/2016JB013883.

Received 20 DEC 2016
Accepted 11 FEB 2017
Accepted article online 15 FEB 2017
Published online 11 MAR 2017

Reconstruction of coseismic slip from the 2015 Illapel earthquake using combined geodetic and tsunami waveform data

Amy Williamson[1], Andrew Newman[1], and Phil Cummins[2]

[1]School of Earth and Atmospheric Sciences, Georgia Institute of Technology, Atlanta, Georgia, USA, [2]Research School of Earth Sciences, Australian National University, Canberra, Australian Capital Territory, Australia

Abstract On 16 September 2015, a moment magnitude (M_w) 8.3 earthquake struck off the coast of central Chile, generating a large tsunami with nearby coastal wave heights observed on tide gauges in Chile and Peru of up to 4.7 m and distal observations of over 40 cm in the Kuril Islands across the Pacific Ocean. Through a transcoastal geodetic study, including tsunami time series recorded at open ocean pressure gauges, subaerial deformation observed through interferometric synthetic aperture radar from the Sentinel-1 A satellite and continuous GPS, we identify the location and extent of coseismic slip. We find that most coseismic slip was concentrated in a patch immediately offshore, with little modeled slip near the trench. This result satisfies the tsunami waveforms measured in the deep ocean north of the rupture area, with wave heights up to 10 cm. While the event exhibits some features of a slow tsunami earthquake (moderately large tsunami and possible slow second-stage rupture), our inversion results do not require substantial near-trench rupture. However, the prevalence of large and shallow thrust along subduction megathrusts along central Chile raises the question of the likelihood of future such events and the implications for future hazardous tsunamigenic earthquakes.

1. Introduction

Over the past century, the Peru-Chile trench has produced many great tsunamigenic earthquakes and has been the focus of several studies of subduction zone earthquake excitation, tectonic strain accumulation, and interseismic coupling [*Vigny et al.*, 2009; *Moreno et al.*, 2010, 2011]. This propensity for large events is in part fueled by the region's rapid plate motion. In the vicinity of central Chile, the Nazca plate subducts beneath the South American plate with a rate of convergence of 74 mm/yr [*DeMets et al.*, 2010]. Many of the more recent earthquakes in the region have produced tsunamis that have been recorded at coastal tide gauges as well as at deep ocean pressure sensors as shown in Figure 1.

One problem in determining the extent of slip from megathrust events is having a clearly resolved domain that extends past the coast to the trench. This shallow, submarine zone is oftentimes poorly resolved through purely geodetic data sets, where many different rupture models can provide equally satisfactory fits to observed data. However, the inclusion of tsunami data, particularly as recorded away from the source at deep ocean pressure gauges, adds a resolvability in this shallow zone that is sensitive to tsunami excitation.

The tsunami generated from a large earthquake is a function of the amount of slip occurring underwater, which for many cases translates to the amount of slip occurring within a shallow (<30 km depth) part of the megathrust. Tsunami waveforms are therefore a good proxy for understanding this shallow, near-trench environment, which for many regions lacks direct observation by instrumentation. This can be particularly important for a special subclass of earthquakes, aptly named tsunami earthquakes, which generate a much larger tsunami than expected from the derived magnitude, and are often deficient in radiating seismic energy while maintaining a characteristically slow rupture propagation [*Kanamori*, 1972]. The 1996 Chimbote, Peru earthquake, with a M_w of only 7.8, produced 1 m level waves locally around Peru and Northern Chile and waves up to 0.3 m near Easter Island, approximately 3800 km away, with up to a maximum runup height of almost 5 m. The disproportionately large tsunami generated by this event is partially a function of its rupture along the shallow part of the megathrust [*Heinrich et al.*, 1998]. Its source location and its deficiency in radiating high-frequency energy led this event to be categorized as a tsunami earthquake by *Newman and Okal* [1998].

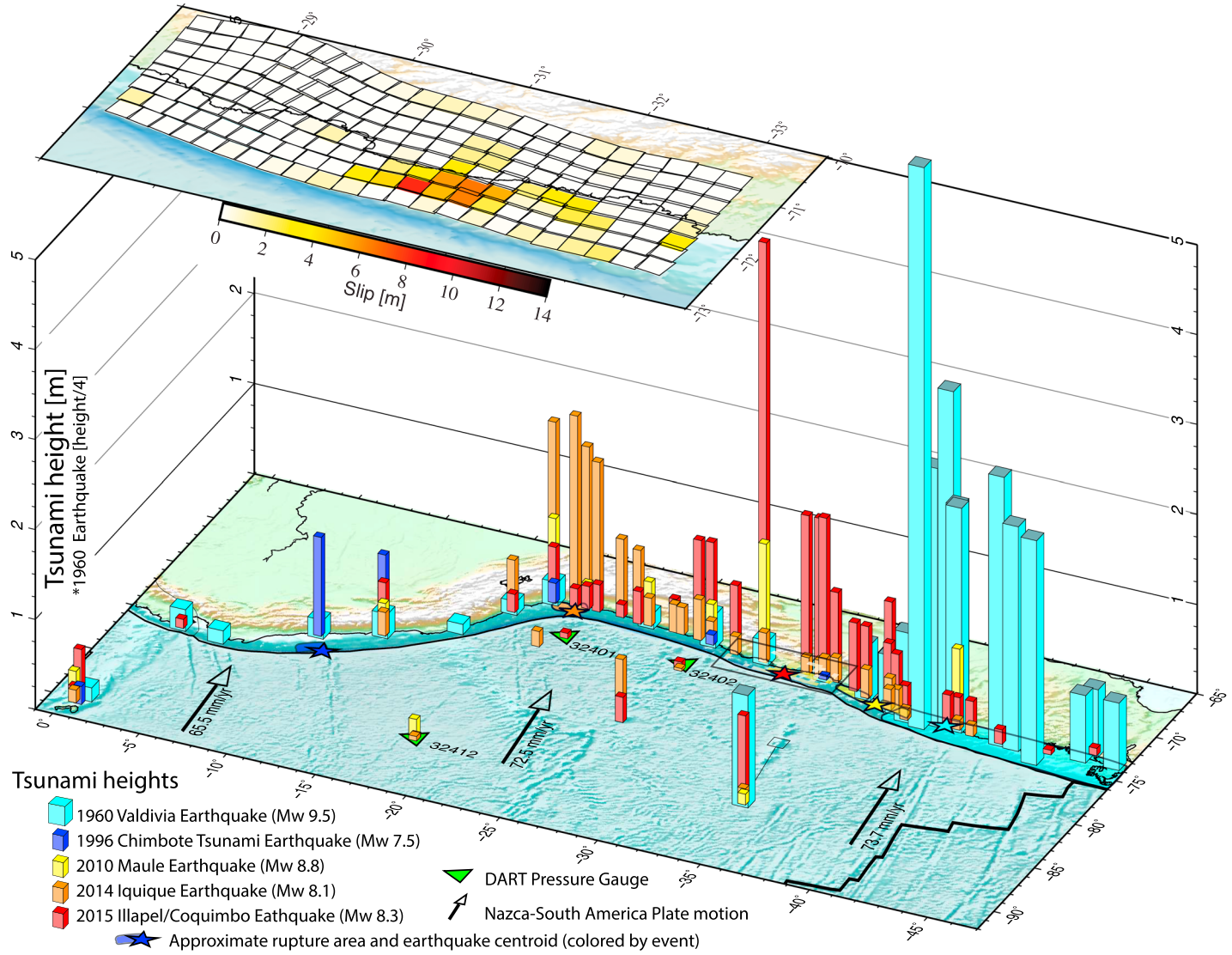

Figure 1. Regional map of past tsunamigenic earthquakes and their generated tsunamis. The epicenter of the 1960 and centroid location for later events [*Ekström et al.*, 2012] with the approximate rupture area are shown by colored stars and transparent polygons beneath [*Bourgeois et al.*, 1999; *Lorito et al.*, 2011; *Hayes et al.*, 2014]. For each event, the regional tsunami wave height measured by local tide gauges and deep water pressure sensors (green triangles) are shown as columnar bars (1960 is augmented by eyewitness accounts (gray tops and are all divided by 4 to stay on scale) [*NGDC*, 2016]. The Nazca plate motion relative to a stable South American plate is also shown (black arrows) [*DeMets et al.*, 2010]. Inset figure: preferred fault plane solution using GPS, InSAR, and tsunami data sets.

However, other tsunamigenic earthquakes in this region were recorded transoceanically without falling into the tsunami earthquake subclass. The largest ever instrumentally recorded earthquake, occurring near Valdivia, Chile, in 1960, generated a large and devastating transoceanic tsunami. Eyewitness observations near the source region suggest 10 to 15 m waves along the coast [*National Geophysical Data Center database* [*NGDC*], 2016]. On a regional scale, tide gauge recordings near the city of Concepción topped out with zero-to-crest amplitudes of over 2.5 m and tide gauges in northern Chile and Peru (2000 to 3000 km away) recorded waves between 0.5 and 1 m in height [*NGDC*, 2016].

More recently, the 2010 M_w 8.8 Maule earthquake ruptured a patch of the megathrust just to the north of the 1960 Valdivia earthquake. In the near field, tide gauges recorded waves with amplitudes around 1 m, with the largest wave = 1.3 m occurring in a bay near the city of Coquimbo. Far-field recordings in Peru were less than 0.5 m. Maximum on-land runup heights reached 29 m at Tirua, 250 km from the source region. Nevertheless, the earthquake and tsunami created over 30 billion dollars in damage and resulted in over 500 causalities in

Chile [*American Red Cross Multi-Disciplinary Team*, 2011; *Fritz et al*., 2011]. Additionally, in 2014, the M_w 8.1 Iquique earthquake in northern Chile, while smaller, also produced a regionally observable tsunami [*An et al*., 2014; *Gusman et al*., 2015].

The latest tsunamigenic addition to the Peru-Chile catalog is the 16 September 2015 M_w 8.3 Illapel earthquake. This event nucleated offshore from Coquimbo Province (approximately 31.57°S and 71.67°W) at approximately 22:54:32 UTC. While the earthquake was smaller in size compared to other contemporary tsunamigenic earthquakes near Chile, including the 2010 Maule earthquake just to the south, it produced a locally large tsunami (up to 4.7 m near Coquimbo as measured by a local tide gauge). The tsunami was transoceanic, with tide gauges recordings throughout the Pacific basin, including Oahu, Hawaii (0.23 m); Kuril Islands, Russia (0.44 m); and Aburatsu, Japan (0.22 m).

The wide spectrum of tsunami generated by earthquakes on the Peru-Chile trench provides a rich and often underutilized data set for static source inversions. While previous studies of the Illapel earthquake have incorporated data from the tsunami, either from the nearby deep ocean pressure gauges or the numerous tide gauges along the coast, this data have been used exclusively through forward models as a constraint on seismic or geodetic inversions or as a validation of a particular model [*Calisto et al*., 2016; *Heidarzadeh et al*., 2016; *Li et al*., 2016; *Tilmann et al*., 2016]. However, for many model results, the forward projection of the model results as a tsunami and its comparison to the observed data from deep ocean gauges is out of phase with observations by a few minutes and often miscalculates the peak amplitude of the first wave, as was shown well in *Calisto et al*. [2016]. While it is unlikely for any one model to well fit all data sets, this consistent phase delay should be addressed as it appears to transcend the type of tsunami propagation model used and the handling of the observed data.

To characterize the 2015 Illapel earthquake, we use line-of-sight (LOS) interferometric synthetic aperture radar (InSAR) observations, static offsets from continuous GPS, and tsunami time series from the four nearest Deep Ocean Assessment and Reporting of Tsunamis (henceforth, DART) pressure gauges. As was originally shown in a combined tsunami-InSAR inversion by *Gusman et al*. [2010], we find that the combination of both land-based geodetic and tsunami data sets, which span the shoreline, allows for maximum resolution of the earthquake slip environment across the subduction megathrust. As we detail below, through a joint inversion of both data types, we find that the maximum coseismic slip occurred in the downdip near-coastal environment, providing the best fit in phase and amplitude to deep ocean time series and on-land static deformation. This moves the locus of dominant slip away from the near-trench environment. While this provides a better fit to the tsunami data, it is in contradiction to some past geodetic and seismic studies on the same event [*Heidarzadeh et al*., 2016; *Lee et al*., 2016; *Li et al*., 2016; *Ruiz et al*., 2016; *Ye et al*., 2016].

2. Data

In this study we incorporate data from four nearby DART pressure gauges. Each gauge records the pressure of the overlying water column and translates this to water column height using a conversion constant at 15 min, 1 min, or 15 s sampling frequencies depending on if each gauge is in standby or a triggered event mode. With a sensitivity of less than 1 mm in deep water, DART pressure gauges are ideal for measuring long period, low-amplitude tsunami waves. Unlike coastal tide gauges which record the tsunami as it interacts with the coastline, leading to nonlinear effects such as harbor resonance, DART gauges, because they are located in the deep ocean, are largely immune to small-scale bathymetric changes. We removed tides recorded at each station through polynomial fitting then filtered the signals to remove high-frequency surface wave energy. Additionally, we windowed each time series to only include the tsunami's arrival and first wavelength in the signal used for the inversion. This is of particular importance for the two nearest stations, where waves reflected from the coast appear early on in the time series.

We also use the LOS displacement field derived from a pair of descending track scenes (24 August and 17 September 2015) recorded by the Sentinel-1A SAR satellite and processed by the European Space Agency [*Prats-Iraola et al*., 2016]. The resultant InSAR image shows a maximum of 150 cm of ground deformation in the LOS direction. While we correct for changes in LOS look angle, we also tested a constant angle of 41° off nadir, near the maximum deformation, and found the difference to be negligible.

Because the data density and interdependence of pixels is extremely high (on the order of 10^7 pixels per image), it was necessary for us to downsample the field of data to make the image manageable for

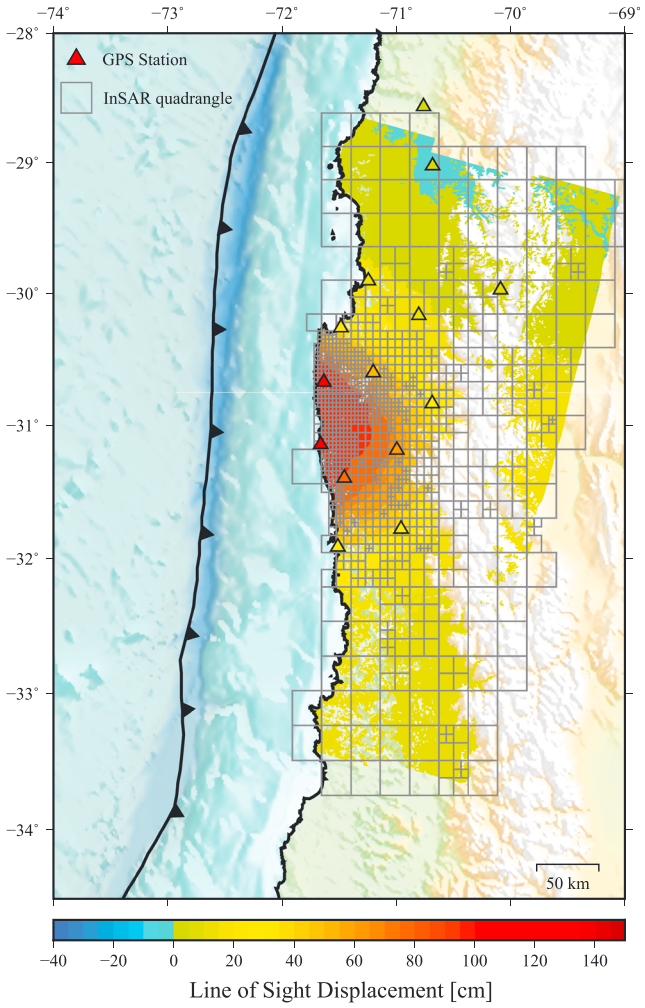

Figure 2. Regional InSAR-derived displacements in the direction of satellite line of sight with Quadtree discretization (grey boxes). Each box represents one point used in the inversion. Triangles indicate the location of the nearby GPS stations. The color of each triangle is the magnitude of displacement of the three-component GPS when translated into the line-of-sight direction. The matching colors between the InSAR displacement field and the GPS show that both data sets are consistent with each other.

computational inversions. To do so, we use a two-dimensional Quadtree decomposition similar to *Jónsson et al.* [2002] that retains more information in environments that have more significant change. We require that each geographically oriented quadrangle containing InSAR signals is split into four smaller quadrangles whenever the variance in LOS displacement is greater than a set tolerance level (5% difference). For the remaining 1200 boxes, we assign the average displacement to the "center of mass" position of coherent pixels. The resulting downsampled image, overlaying the original displacement field, is shown in Figure 2. Because the second pass follows 1 day after the event, any postseismic signal is likely to remain small. Furthermore, because most observations of early afterslip occur primarily updip of the main rupture along subduction zones [e.g., *Hsu et al.*, 2006; *Malservisi et al.*, 2015], we suspect the land-based data to be more representative of coseismic rupture.

Additionally, we incorporate static offsets from 16 three-component continuous GPS stations, located in central Chile, operated by the National Seismological Center of the Universidad de Chile, with static displacements reported in *Ruiz et al.* [2016]. The data set shows a consistent seaward motion by all stations and a small but complex and comparably small vertical signal of uplift and subsidence at the coastal stations.

When constrained to the use of only land-based geodetic instruments such as GPS and InSAR, the shallow subduction zone region is generally too far offshore to be resolvable in distributed-slip (i.e., "finite fault") inversions. While seafloor geodetic instruments are feasible, they are often cost prohibitive and thus few regions currently have the infrastructure in place, causing many communities to forgo their use [*Newman*, 2011]. This leads to difficulty in constraining slip in this highly hazardous, but in these cases poorly resolved, zone. By supplementing this data set with ocean-based observations, like tide gauge or pressure gauge time series, we find that spatial resolvability of the offshore region increases substantially (see section 3.3, below).

3. Methods

3.1. Model Geometry

We describe the source region with a three-dimensional curviplanar fault geometry. We then discretize the modeled fault plane into a 575 × 200 km surface, consisting of a 23 × 8 grid, with individual patches of

dimensions 25 km along strike and 25 km along dip. The strike and dip of the fault interface vary for each patch, approximating the profile created from Slab 1.0 [*Hayes et al*., 2012]. While the inclusion of a strike variability does cause a small amount of overlap of patches, the total overlap is negligible in calculating the seismic moment.

3.2. Inversion Technique

We calculate Green's functions for InSAR LOS displacements and GPS static offsets through an analytic solution to the elastodynamic equations for rectangular dislocations in an elastic half-space [*Okada*, 1985]. For DART data, we generate Green's functions relating fault slip by combining the vertical surface deformation from *Okada* [1985] with the tsunami propagation model, JAGURS [*Baba et al*., 2015; *Allgeyer and Cummins*, 2014]. JAGURS is a finite difference method model that, in addition to solving the nonlinear shallow water wave equations, has the ability to incorporate elastic loading, seawater compressibility, gravitational potential change, and Boussinesq dispersion into the propagation simulation. In order to account for hydrodynamic effects that alter the pattern of displacement transmitted from the seafloor to sea surface, we applied a smoothing filter [*Kajiura*, 1963] to the seafloor displacement of each subfault before it was translated to the sea surface. Finally, we perform a linear inversion for positive dip-slip motion (thrust) along our fault geometry, bounding to be less than 20 m per fault patch. While the tsunami propagation code is nonlinear, it is well behaved for open ocean tsunami propagation, particularly in the near field, making it amenable for inclusion in a bound linear inversion.

We relate our geodetic and tsunami Green's functions to fault interface slip through the model GTdef developed by *Chen et al*. [2009] and following *Jónsson et al*. [2002]. The model solves the linear system of equations using

$$\begin{bmatrix} w\,d \\ 0 \end{bmatrix} = \begin{bmatrix} w\,G \\ \kappa^2 D \end{bmatrix} \mathrm{m}$$

where d is the observed data vector, G is the Green's function matrix, m is the vector of unknown slip on the fault, and D is a finite difference smoothing operator that relates each patch with a weight regulated by κ. The Green's function matrix is composed of tsunami waveforms and static offsets from both LOS InSAR measurements and horizontal and vertical GPS measurements. Both the observation vector and the Green's function matrix are modified with a coefficient, w, representing measurement errors associated with each type of observation and a weight relating the different data sets. The total contribution of each data set varies, with the number of discretized tsunami waveform data (10,800 points) exceeding Quadtree downsampled InSAR data (1200 points) and GPS data (16 sites $\times$ 3 components). To ensure comparable sensitivity between the tsunami and land-based geodetic data, we weighted the cumulative data sets equally for the inversion.

We regularize our solution using κ to force an interdependence between adjacent slip patches [*Harris and Segall*, 1987]. An increasing smoothing factor, acts as a trade-off with the misfit of the model. The misfit is determined as the root-mean-square of the weighted-residual sum of squares. While an unconstrained model where each patch acts independently of its surrounds would theoretically provide the best fit to the observed data, solutions would be nonunique and would potentially provide unrealistically rough results. Instead, we evaluate a range of unique models constrained by increasing κ (Figure S1 in the supporting information), before choosing our preferred model, determined by evaluating the trade-off between model misfit and roughness.

3.3. Model Resolution

We approximate the spatial resolvability of our model using a "checkerboard test," consisting of 50 km by 50 km blocks with alternating predefined uniform slip magnitudes between 0 and 1 m (Figure 3). Using these patches as input, we predict deformation at each data point for InSAR, GPS, and tsunami data sets as well as the combination of all three. We subsequently invert these synthetic data with our observed data error and compare our inverted with our initial models. In areas where the checkerboard is retained, we have high resolvability.

The spatial resolution of the study region is assumed to vary due to a nonuniform distribution of observations. For geodetic (InSAR and GPS) checkerboard results, the best resolution is centered at 71.5°W and 31°S,

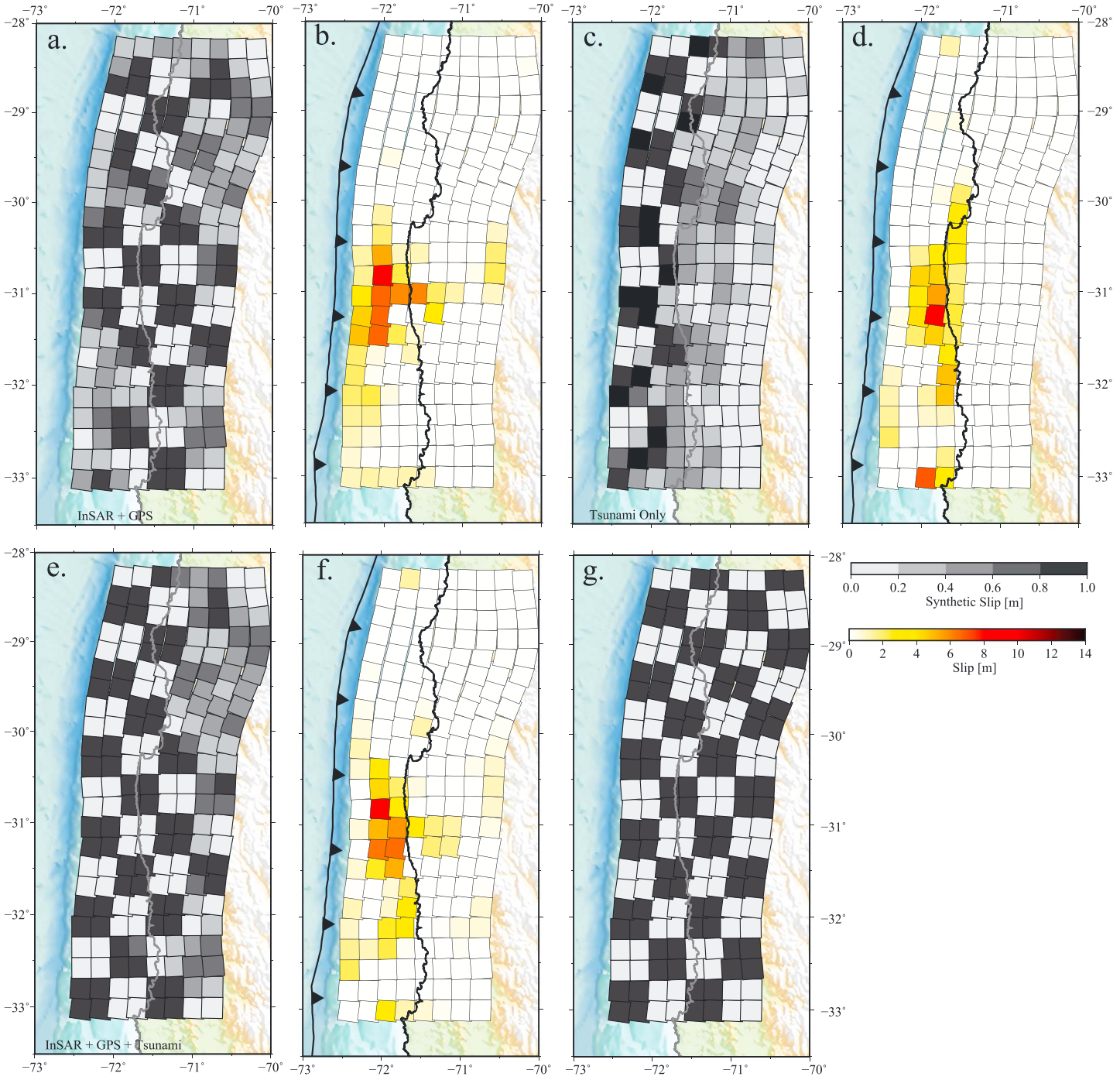

Figure 3. "Checkerboard" resolution tests. (a) Geodetic only checkerboard solution, using only the InSAR and GPS data sets. (b) Preferred model results from an InSAR and GPS data set. (c) Checkerboard solution incorporating only DART tsunami waveforms. (d) Preferred model results from a tsunami data set. (e) Checkerboard solution using all available data. (f) Preferred slip solution using all data. (g) Initial checkerboard input with 50 × 50 km checkers alternating between 0 and 1 m of dip slip. Solutions in Figures 3b and 3c illustrate the spatial variability and limitations of using geodetic and tsunami data sets, respectively.

about where the largest change in deformation both in InSAR and GPS offsets occurs. However, resolution is limited offshore and does not extend along strike through the study area. The tsunami data set checkerboard result shows an excellent recreation of the checkerboard pattern offshore, but resolution is quickly lost for fault patches located under land, where slip would minimally affect the water column. The checkerboard for the combined data set has good resolution for almost the entire study region, excluding a

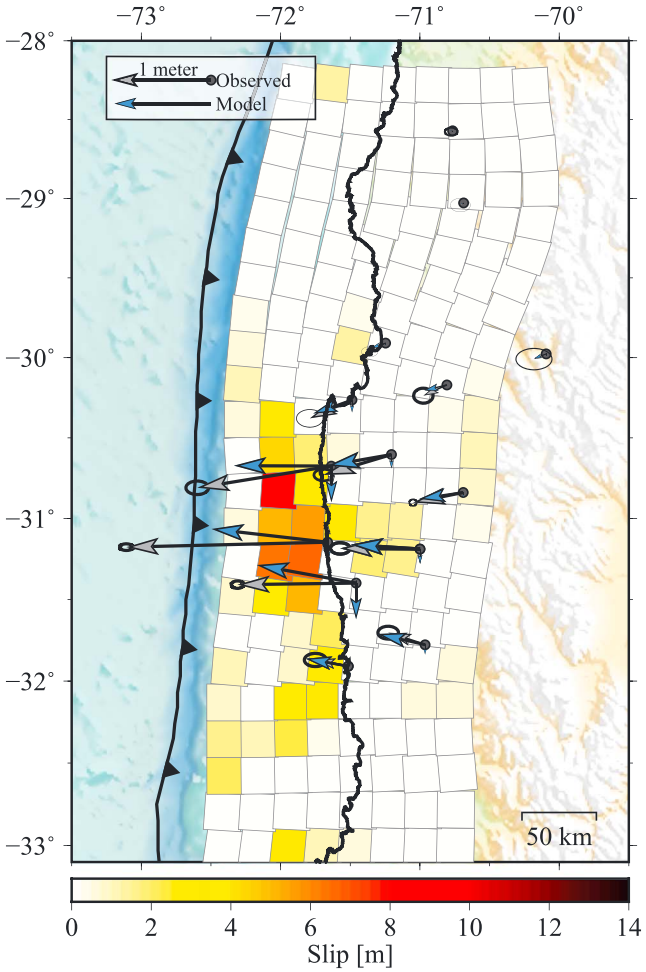

Figure 4. Observed (gray) and modeled (blue) horizontal and vertical coseismic GPS coseismic displacements superimposed on the preferred slip model (repeated from Figure 3f).

patch downdip and to the north of the main region of deformation, where there are few GPS stations and a small amount of change in the InSAR image, thus a smaller data set. However, for the combination image, the checkerboard pattern was recovered for the region where we expect to see most slip from this earthquake.

4. Results

The majority of slip occurred in one main patch immediately offshore but not reaching the trench axis. The peak slip in our preferred model reaches 11 m, while the main patch of consistent slip extends about 125 km along strike and 50 km along dip. This peak slip measurement is an estimate of the slip in the smoothed model; the value has the potential to change with a different smoothing factor. Forward projections of the GPS displacement vectors, InSAR LOS displacement fields, and tsunami waveforms are shown in Figures 4–6.

Our model is in good agreement with tsunami time series recorded at four nearby DART gauges (Figure 5), with little phase delay between the modeled tsunami arrival and the observed time series, and a consistent peak amplitude for the initial part of the tsunami, before the inclusions of coastal reflections. The fit of the model at the nearest gauge, DART 32402, also partially recreates the wave trough that was recorded about 50 min after the earthquake. This feature was not modeled in studies assessed in *Calisto et al*. [2016], *Heidarzadeh et al*. [2016], or *Tang et al*. [2016]. While the later, trailing part of the tsunami is not consistently recreated across all DART gauges, this part of the time series includes modulations of the tsunami from coastal reflections and inundation, which we do not confidently recreate in our tsunami Green's functions or forward tsunami model.

Forward projections of the geodetic data, both for the GPS stations and a recreation of the InSAR deformation, both yield good results. The largest misfit within the geodetic data sets occurs close to the coastline where the preferred model slightly underpredicts deformation.

5. Discussion

The addition of a tsunami data set to the earthquake source inversion adds a spatial resolution to the solution, especially in the near-trench region. This is noticeable when comparing the arrival times of a tsunami at deep water gauges between models and observations. The inclusion of tsunami data sets also assists in constraining shallow slip, which may not be resolved well with land-based data sets, and may also constrain seafloor uplift in a complex and often poorly understood part of the subduction zone.

This region has poor azimuthal coverage of DART gauges; they are only located to the north of the rupture area and oblique to the directivity of the tsunami. While a new station was added directly south of the

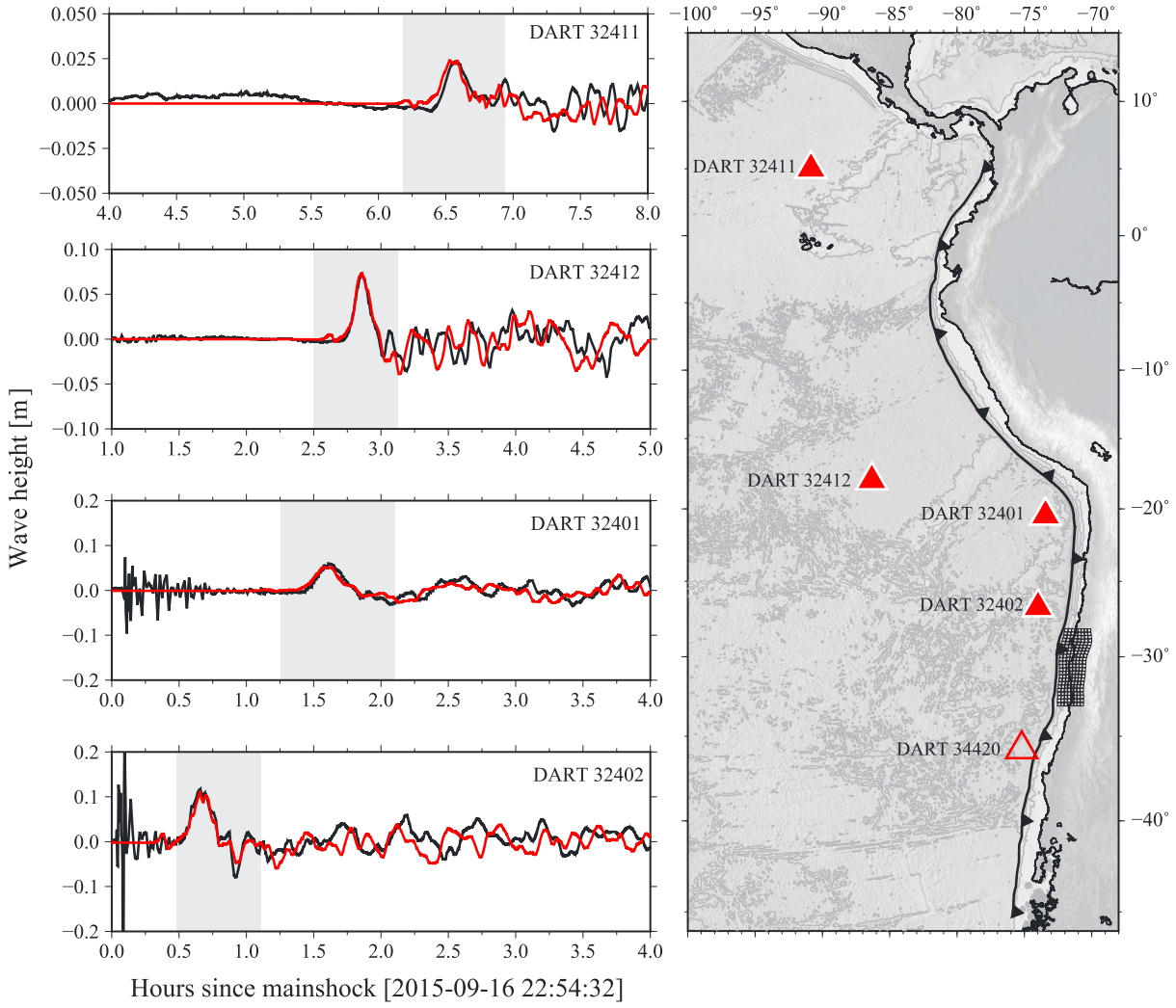

Figure 5. (left column) Black line: recorded tsunami waveforms from the four nearest and active DART pressure gauges with timing relative to the main shock. Red line: forward simulated tsunami result for preferred model. The gray boxes in each of the four subplots highlight the windowed region used in the inversion process. Regions were picked to include the first and largest amplitude part of the tsunami while excluding surface wave recordings and later coastal reflections. Both of the excluded effects cannot be modeled through our inversion process. (right) Geographic distribution of nearby DART gauges active during the earthquake (red solid triangles). The discretized fault plane is shown near 30°S. The hollow triangle outlined in red is the newest addition to the DART gauge fleet along the Peru-Chile trench but was not active during the tsunami.

Illapel earthquake during the fall of 2015, which could potentially aid in constraining the location of slip with further confidence, it was not fully deployed until after the event. Located near the trench axis, the close proximity of the gauge to the megathrust reduced the delay between the earthquake and the arrival of the tsunami at the station, increasing the time available to assess the tsunami for far-field hazard warnings. It also provides an opportunity for real-time or near-real-time source inversions incorporating tsunami data and possibly supplementing other real-time source characterization methods [*Benavente et al.*, 2016].

Ideally, the inclusion of transoceanic DART stations can aid in the modeling of offshore slip through additional observations over a wider azimuth range. However, this also requires the inclusion of the accumulating effects of dispersion and possibly the elastic loading of the seafloor from the propagating wave. These effects not only change the arrival time of the wave at far-field stations, when compared to linear longwave models, but also distort the waveform itself [*Watada et al.*, 2014]. While it is possible to address some of these distortions [e.g., *Watada et al.*, 2014], we exclude use of the far-field tsunami waveforms because they are expected to have much less sensitivity to the details of the slip distribution than the near-field waveforms used here [*Geist and Dmowska*, 1999].

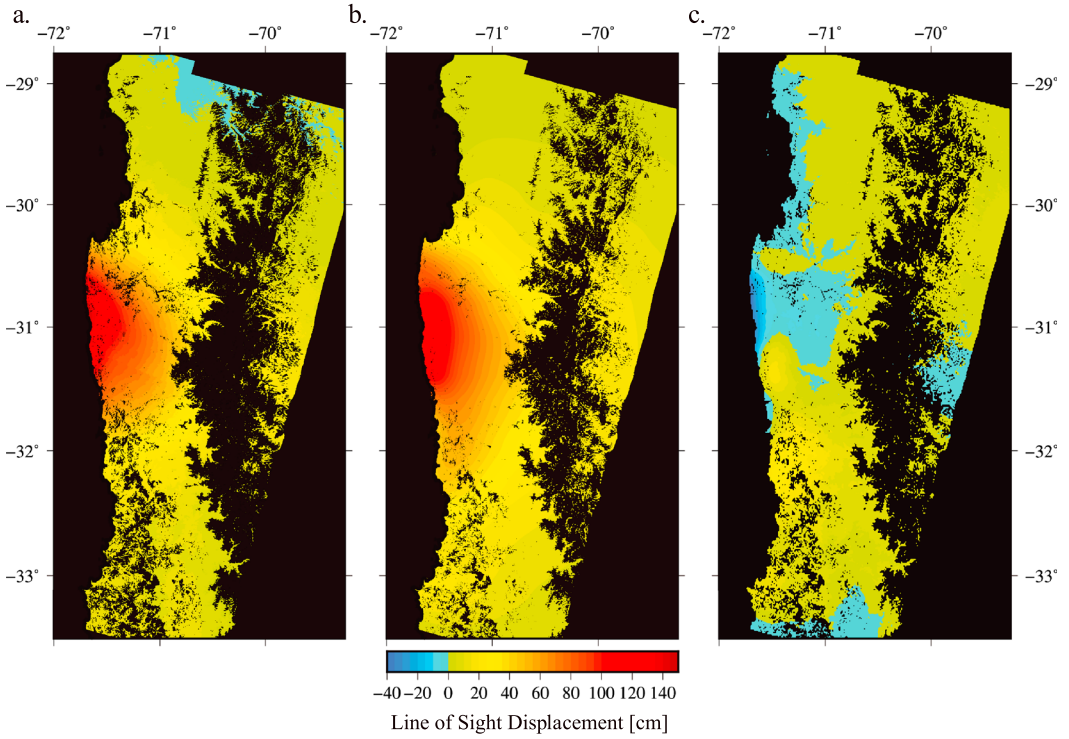

Figure 6. Comparison of InSAR line-of-sight (LOS) change for data and our preferred model. (a) Observed LOS displacement, repeated from Figure 2. (b) LOS projection of the preferred model results. (c) Residual LOS displacement, determined by removing the predicted (Figure 6b) from the observed (Figure 6a) signal.

Most earthquakes exhibit rupture speeds up to 3 km/s in subduction zone environments [e.g., *Bilek and Lay*, 1999]. However, in the case of slow, tsunami earthquakes, rupture can be substantially reduced, down to as little as 1 km/s, greatly extending the duration of rupture [*Kanamori*, 1972], and substantially diminishing the propagated energy, as was the case in the 1996 Chimbote, Peru earthquake (Figure 1) [*Newman and Okal*, 1998]. The slowed rupture is sometimes attributed to slip in the shallowest portion of the interface near the trench [e.g., *Bilek and Lay*, 1999; *Polet and Kanamori*, 2000]. Based on teleseismic energy backprojections, *Yin et al*. [2016] identified a substantial and slow delayed rupture component to the 2015 Illapel earthquake, extending between 80 and 130 s from the initial rupture, with the patch occurring updip of the initial nucleation and very near the trench. Using a teleseismic inversion of the spectral contributions from the Illapel earthquake, *Lee et al*. [2016] similarly found a two-stage rupture process but with moderately longer durations, the first lasting 100 s and the second not terminating until about 250 s after the rupture initiation.

Examination of the real-time radiated energy growth, automatically ran at Georgia Tech using RTerg [*Convers and Newman*, 2011], shows that this earthquake does indeed exhibit complex and delayed energy release that is discernable within the cumulative growth of high-frequency (0.5–2 Hz) teleseismically radiated *P* wave energy (Figure 7). While the automated algorithm estimated the rupture duration, T_R, at 135 s using the crossover between the rapid initial growth and the later slow growth of high-frequency energy, the steeply sloped growth phase uncharacteristically exhibits a break in the linear slope. Unlike most other earthquakes which exhibit a simple singular growth phase, this event has a more rapid growth period that terminates at 83 s, followed by a more slowly growing phase that terminates near 146 s. *Newman et al*. [2011], using the 2010 Mentawai tsunami earthquake, identified that such a depressed growth is a characteristic of slow rupture. Interestingly, these windows correspond well with the two periods found by *Yin et al*. [2016] that also identified the second stage as growing more slowly. Furthermore, the real-time energy result culminated in a high-frequency energy magnitude, $M_{e\_hf} = 7.8$ (corresponding to 3.0E15 J), 0.5 units smaller than M_w (8.3) as reported by the Global Centroid Moment Tensor Catalog (gCMT). Such a feature is comparable to the deficiency in the theta parameter ($\Theta = \log_{10}(E/M_0)$), originally described as characteristic for slow tsunami earthquakes in *Newman and Okal* [1998]. Thus, while our joint inversion that includes DART data suggests the most

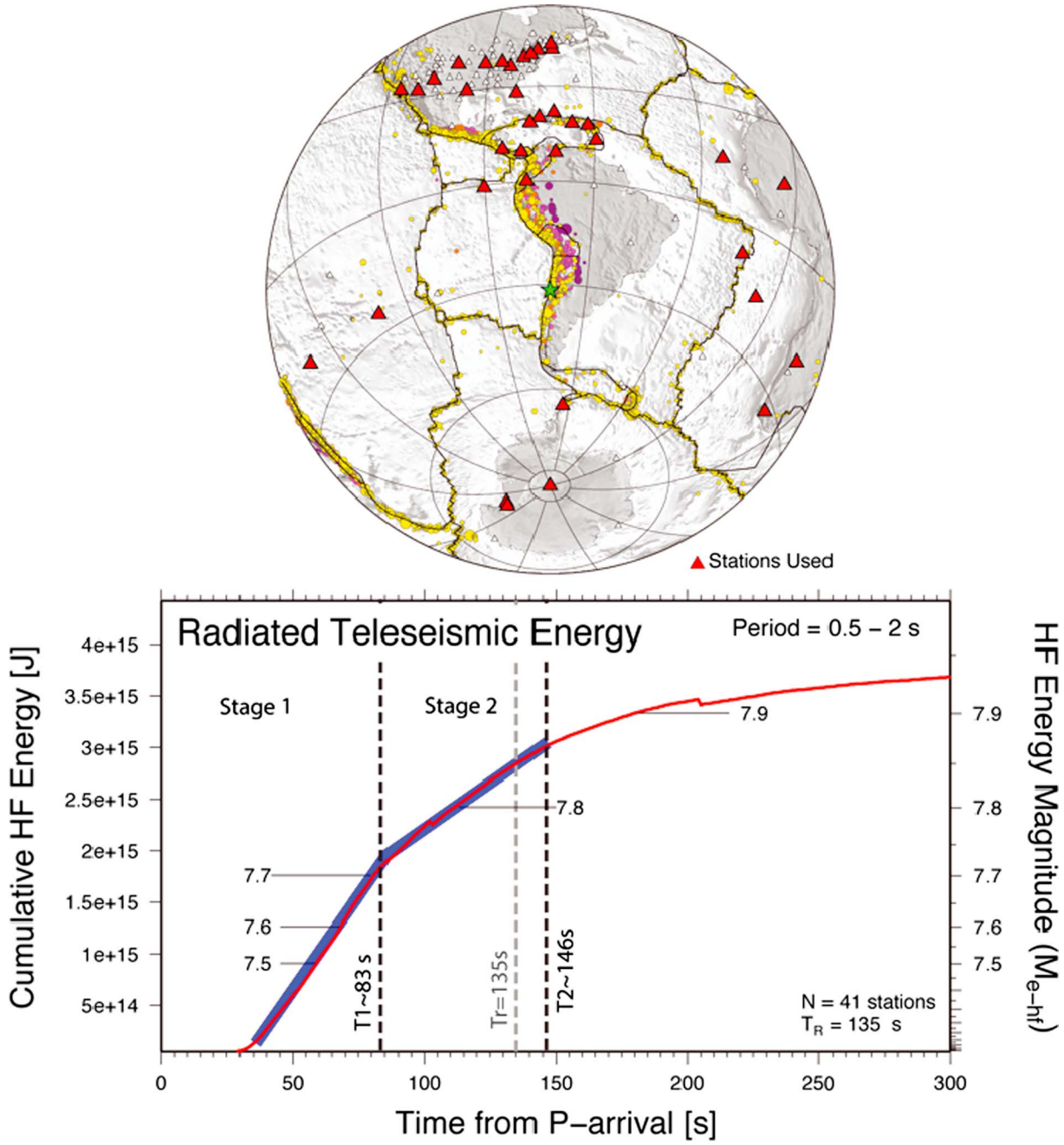

Figure 7. The cumulative high-frequency energy radiated from the Illapel earthquake is shown (red line) using data from 41 seismic stations available in real time (red triangles in map) and automatically processed following *Convers and Newman* [2011]. The automated rupture duration, T_R (dashed gray line), two near-linear periods of growth (denoted by thick blue lines), and their termination times relative to the earthquake nucleation (dashed black lines). The cumulative energy is converted to a high-frequency energy magnitude, which appears deficient for this event, similar but more moderate than slow-rupturing tsunami earthquakes.

updip component of the megathrust is not responsible for the tsunami generated, a number of results strongly support the likelihood of a slowed and possibly near-trench component: (1) the backprojections of *Yin et al*. [2016], (2) the spectral analysis of *Lee et al*. [2016], and (3) the slowed secondary growth and reduced overall earthquake energy following *Convers and Newman* [2011]. While it is likely that the second and slowed phase of energy release contributed to the overall tsunami, it is not clear that significant fractions of the slip for this component occurred near the trench. If the slowed phase did occur near the trench, it is possible that the dip angle is so low that it had an inappreciable contribution to tsunami generation.

6. Conclusion

We conduct a transcoastal joint inversion to solve for coseismic slip along the subduction megathrust using deep ocean pressure gauge tsunami time series, continuous GPS, and Sentinal-1A InSAR data following the 2015 Illapel earthquake. By supplementing the traditional land-based geodetic slip inversion with a tsunami data set, key information about the region between the trench and the coast can be incorporated, substantially increasing the resolution domain for megathrust events. Our preferred result has a large concentration of slip near the coastline and downdip from the trench axis, but still under a submarine environment, leading to tsunami excitation. Our model is in good agreement with tsunami time series recorded at four nearby DART gauges, with little phase delay between the modeled tsunami arrival and the observed time series, and a consistent peak amplitude for the initial part of the tsunami, before the inclusions of coastal reflections. Unlike other models, this result does not require the earthquake to rupture the near-trench region of the megathrust in order to fit the timing or magnitude of the observed tsunami. The incorporation of tsunami data into the inversion processes provides a useful data set for constraining offshore slip in a region that is otherwise difficult to resolve through geodetic means. Consistent use of tsunami data, when available, for future earthquakes will allow for a clearer understanding of when there is and is not shallow slip on the megathrust. When applied, this data allow for a better assessment of the diverse tsunamigenic behavior of earthquakes along the Peru-Chile trench and can also be included in studies of other seismically active regions.

Acknowledgments

This research was supported through State Funds through Georgia Tech to A.V.N. as well as through the National Science Foundation East Asian and Pacific Summer Institute project 1614142. P. Cummins was partially supported by Australian Research DP120103297. Figures were generated using Generic Mapping Tools from *Wessel et al*. [2013]. We appreciate the processed Sentinel-1 data from the Copernicus Service (collected in 2015) available at the InSARap Project site (http://insarap.org/) and the open ocean tsunami waveform data made accessible by the U.S. National Oceanic and Atmospheric Administration (available at http://nctr.pmel.noaa.gov/Dart/). GPS data were recorded by the National Seismological Center of the Universidad de Chile and processed by J.C. Baez. Finally, we thank Emma Hill and two anonymous reviewers for their constructive comments.

References

Allgeyer, S., and P. Cummins (2014), Numerical tsunami simulation including elastic loading and seawater density stratification, *Geophys. Res. Lett.*, *41*, 2368–2375, doi:10.1002/2014GL059348.

An, C., I. Sepúlveda, and P. L. F. Liu (2014), Tsunami source and its validation of the 2014 Iquique, Chile Earthquake, *Geophys. Res. Lett.*, *41*, 3988–3994, doi:10.1002/2014GL060567.

American Red Cross Multi-Disciplinary Team (2011), Report on the 2010 Chilean earthquake and tsunami response, *U.S. Geol. Surv. Open File Rep., 2011–1053, 1.1*, 68 pp. [Available at https://pubs.usgs.gov/of/2011/1053/.]

Baba, T., N. Takahashi, Y. Kaneda, K. Ando, D. Matsuoka, and T. Kato (2015), Parallel implementation of dispersive tsunami wave modeling with a nesting algorithm for the 2011 Tohoku Tsunami, *Pure Appl. Geophys.*, *172*(12), 3455–3472.

Benavente, R., P. R. Cummins, and J. Dettmer (2016), Rapid automated W-phase slip inversion for the Illapel great earthquake (2015, M_w = 8.3), *Geophys. Res. Lett.*, *43*, 1910–1917, doi:10.1002/2015GL067418.

Bilek, S. L., and T. Lay (1999), Rigidity variations with depth along interplate megathrust faults in subduction zones, *Nature*, *400*(6743), 443–446.

Bourgeois, J., C. Petroff, H. Yeh, V. Titov, C. E. Synolakis, B. Benson, J. Kuroiwa, J. Lander, and E. Norabuena (1999), Geologic setting, field survey and modeling of the Chimbote, Northern Peru, tsunami of 21 February 1996, in *Seismogenic and Tsunamigenic Processes in Shallow Subduction Zones*, pp. 513–540, Birkhäuser, Basel, doi:10.1007/s000240050242.

Calisto, I., M. Miller, and I. Constanzo (2016), Comparison between tsunami signals generated by different source models and the observed data of the Illapel 2015 earthquake, *Pure Appl. Geophys.*, *173*(4), 1051–1061.

Chen, T., A. V. Newman, L. Feng, and H. M. Fritz (2009), Slip distribution from the 1 April 2007 Solomon Islands earthquake: A unique image of near-trench rupture, *Geophys. Res. Lett.*, *36*, L16307, doi:10.1029/2009GL039496.

Convers, J. A., and A. V. Newman (2011), Global evaluation of large earthquake energy from 1997 through mid-2010, *J. Geophys. Res.*, *116*, B08304, doi:10.1029/2010JB007928.

DeMets, C., R. G. Gordon, and D. F. Argus (2010), Geologically current plate motions, *Geophys. J. Int.*, *181*(1), 1–80, doi:10.1111/j.1365-246X.2009.04491.x.

Ekström, G., M. Nettles, and A. M. Dziewoński (2012), The global CMT project 2004–2010: Centroid-moment tensors for 13,017 earthquakes, *Phys. Earth Planet. Int.*, *200*, 1–9, doi:10.1016/j.pepi.2012.04.002.

Fritz, H. M., et al. (2011), Field survey of the 27 February 2010 Chile tsunami, *Pure Appl. Geophys.*, *168*(11), 1989–2010, doi:10.1007/s00024-011-0283-5.

Geist, E. L., and R. Dmowska (1999), Local tsunamis and distributed slip at the source, *Pure Appl. Geophys.*, *154*, 485–512.

Gusman, A. R., Y. Tanioka, T. Kobayashi, H. Latief, and W. Pandoe (2010), Slip distribution of the 2007 Bengkulu earthquake inferred from tsunami waveforms and InSAR data, *J. Geophys. Res.*, *115*, B12316, doi:10.1029/2010JB007565.

Gusman, A. R., S. Murotani, K. Satake, M. Heidarzadeh, E. Gunawan, S. Watada, and B. Schurr (2015), Fault slip distribution of the 2014 Iquique, Chile, earthquake estimated from ocean-wide tsunami waveforms and GPS data, *Geophys. Res. Lett.*, *42*, 1053–1060, doi:10.1002/2014GL062604.

Harris, R. A., and P. Segall (1987), Detection of a locked zone at depth on the Parkfield, California, segment of the San Andreas Fault, *J. Geophys. Res.*, *92*, 7945–7962, doi:10.1029/JB092iB08p07945.

Hayes, G. P., D. J. Wald, and R. L. Johnson (2012), Slab1.0: A three-dimensional model of global subduction zone geometries, *J. Geophys. Res.*, *117*, B01302, doi:10.1029/2011JB008524.

Hayes, G. P., M. W. Herman, W. D. Barnhart, K. P. Furlong, S. Riquelme, H. M. Benz, E. Bergman, S. Barrientos, P. S. Earle, and S. Samsonov (2014), Continuing megathrust earthquake potential in Chile after the 2014 Iquique earthquake, *Nature*, *512*(7514), 295–298, doi:10.1038/nature13677.

Heidarzadeh, M., S. Murotani, K. Satake, T. Ishibe, and A. R. Gusman (2016), Source model of the 16 September 2015 Illapel, Chile, M_w 8.4 earthquake based on teleseismic and tsunami data, *Geophys. Res. Lett.*, *43*, 643–650, doi:10.1002/2015GL067297.

Heinrich, P., F. Schindele, S. Guibourg, and P. F. Ihmlé (1998), Modeling of the February 1996 Peruvian tsunami, *Geophys. Res. Lett.*, *25*, 2687–2690, doi:10.1029/98GL01780.

Hsu, Y. J., M. Simons, J. P. Avouac, J. Galetzka, K. Sieh, M. Chlieh, D. Natawidjaja, L. Prawirodirdjo, and Y. Bock (2006), Frictional afterslip following the 2005 Nias-Simeulue earthquake, Sumatra, *Science*, *312*(5782), 1921–1926, doi:10.1126/science.1126960.

Jónsson, S., H. Zebker, P. Segall, and F. Amelung (2002), Fault slip distribution of the 1999 M_w 7.1 Hector Mine, California, earthquake, estimated from satellite radar and GPS measurements, *Bull. Seismol. Soc. Am.*, *92*(4), 1377–1389.

Kajiura, K. (1963), The leading wave of a tsunami, *Bull. Seismol. Soc. Am.*, *41*, 535–571.

Kanamori, H. (1972), Mechanism of tsunami earthquakes, *Phys. Earth Planet. Int.*, *6*(5), 346–359, doi:10.1016/0031-9201(72)90058-1.

Lee, S. J., T. Y. Yeh, T. C. Lin, Y. Y. Lin, T. R. Song, and B. S. Huang (2016), Two-stage composite megathrust rupture of the 2015 M_w8.4 Illapel, Chile, earthquake identified by spectral-element inversion of teleseismic waves, *Geophys. Res. Lett.*, *43*, 4979–4985, doi:10.1002/2016GL068843.

Li, L., T. Lay, K. F. Cheung, and L. Ye (2016), Joint modeling of teleseismic and tsunami wave observations to constrain the 16 September 2015 Illapel, Chile, M_w 8.3 earthquake rupture process, *Geophys. Res. Lett.*, *43*, 4303–4312, doi:10.1002/2016GL068674.

Lorito, S., F. Romano, S. Atzori, X. Tong, A. Avallone, J. McCloskey, M. Cocco, E. Boschi, and A. Piatanesi (2011), Limited overlap between the seismic gap and coseismic slip of the great 2010 Chile earthquake, *Nature*, *4*(3), 173–177, doi:10.1038/ngeo1073.

Malservisi, R., et al. (2015), Multiscale postseismic behavior on a megathrust: The 2012 Nicoya earthquake, Costa Rica, *Geochem. Geophys. Geosyst.*, *16*, 1848–1864, doi:10.1002/2015GC005794.

Moreno, M., M. Rosenau, and O. Oncken (2010), 2010 Maule earthquake slip correlates with pre-seismic locking of Andean subduction zone, *Nature*, *467*(7312), 198–202, doi:10.1038/nature09349.

Moreno, M., et al. (2011), Heterogeneous plate locking in the South–Central Chile subduction zone: Building up the next great earthquake, *Earth Planet. Sci. Lett.*, *305*(3), 413–424, doi:10.1016/j.epsl.2011.03.025.

National Geophysical Data Center database (NGDC) (2016), [Available at https://www.ngdc.noaa.gov] (accessed: 15.05.16).

Newman, A. V. (2011), Hidden depths, *Nature*, *474*(7352), 441–443, doi:10.1038/474441a.

Newman, A. V., and E. A. Okal (1998), Teleseismic estimates of radiated seismic energy: The E/M_0 discriminant for tsunami earthquakes, *J. Geophys. Res.*, *103*, 26,885–26,898, doi:10.1029/98JB02236.

Newman, A. V., G. Hayes, Y. Wei, and J. A. Convers (2011), The 25 October 2010 Mentawai tsunami earthquake, from real-time discriminants, finite-fault rupture, and tsunami excitation, *Geophys. Res. Lett.*, *38*, L05302, doi:10.1029/2010GL046498.

Okada, Y. (1985), Surface deformation due to shear and tensile faults in a half-space, *Bull. Seismol. Soc. Am.*, *75*(4), 1135–1154.

Prats-Iraola, P., et al. (2016), Sentinel-1 tops interferometric time series results and validation, in *Geoscience and Remote Sensing Symposium (IGARSS), 2016, IEEE International*, pp. 3894–3897, doi:10.1109/IGARSS.2016.7730011.

Polet, J., and H. Kanamori (2000), Shallow subduction zone earthquakes and their tsunamigenic potential, *Geophys. J. Int.*, *142*(3), 684–702.

Ruiz, S., et al. (2016), The seismic sequence of the 16 September 2015 Mw 8.3 Illapel, Chile, earthquake, *Seismol. Res. Lett.*, doi:10.1785/0220150281.

Tang, L., V. Titov, C. Moore, and Y. Wei (2016), Real-time assessment of the 16 September 2015 Chile tsunami and implications for near-field forecast, *Pure Appl. Geophys.*, *173*(2), 369–387, doi:10.1007/s00024-015-1226-3.

Tilmann, F., et al. (2016), The 2015 Illapel earthquake, central Chile: A type case for a characteristic earthquake?, *Geophys. Res. Lett.*, *43*, 574–583, doi:10.1002/2015GL066963.

Vigny, C., A. Rudloff, J. C. Ruegg, R. Madariaga, J. Campos, and J. M. Alvarez (2009), Upper plate deformation measured by GPS in the Coquimbo Gap, Chile, *Phys. Earth Planet. Int.*, *175*(1), 86–95, doi:10.1016/j.pepi.2008.02.013.

Watada, S., S. Kusumoto, and K. Satake (2014), Traveltime delay and initial phase reversal of distant tsunamis coupled with the self-gravitating elastic Earth, *J. Geophys. Res. Solid Earth*, *119*, 4287–4310, doi:10.1002/2013JB010841.

Wessel, P., W. H. F. Smith, R. Scharroo, J. F. Luis, and F. Wobbe (2013), Generic mapping tools: Improved version released, *Eos Trans. AGU*, *94*, 409–410, doi:10.1002/2013EO450001.

Ye, L., T. Lay, H. Kanamori, and K. D. Koper (2016), Rapidly estimated seismic source parameters for the 16 September 2015 Illapel, Chile M_w 8.3 earthquake, *Pure Appl. Geophys.*, *173*(2), 321–332.

Yin, J., H. Yang, H. Yao, and H. Weng (2016), Coseismic radiation and stress drop during the 2015 M_w 8.3 Illapel, Chile megathrust earthquake, *Geophys. Res. Lett.*, *43*, 1520–1528, doi:10.1002/2015GL067381.

Supporting information for

Reconstruction of coseismic slip from the 2015 Illapel earthquake using combined geodetic and tsunami waveform data

Amy Williamson[a,*], Andrew Newman[a], Phil Cummins[b]

[a] School of Earth and Atmospheric Sciences, Georgia Institute of Technology, 311 Ferst Drive, Atlanta, GA, 30332, United States
[b]Research School of Earth Sciences, Australian National University, Canberra, ACT, Australia

Contents of this file

Introduction

This supporting information contains further information on the range of fault solutions with variable smoothing parameters as well as our fault plane geometry and optimal solution slip distribution in tabular format.

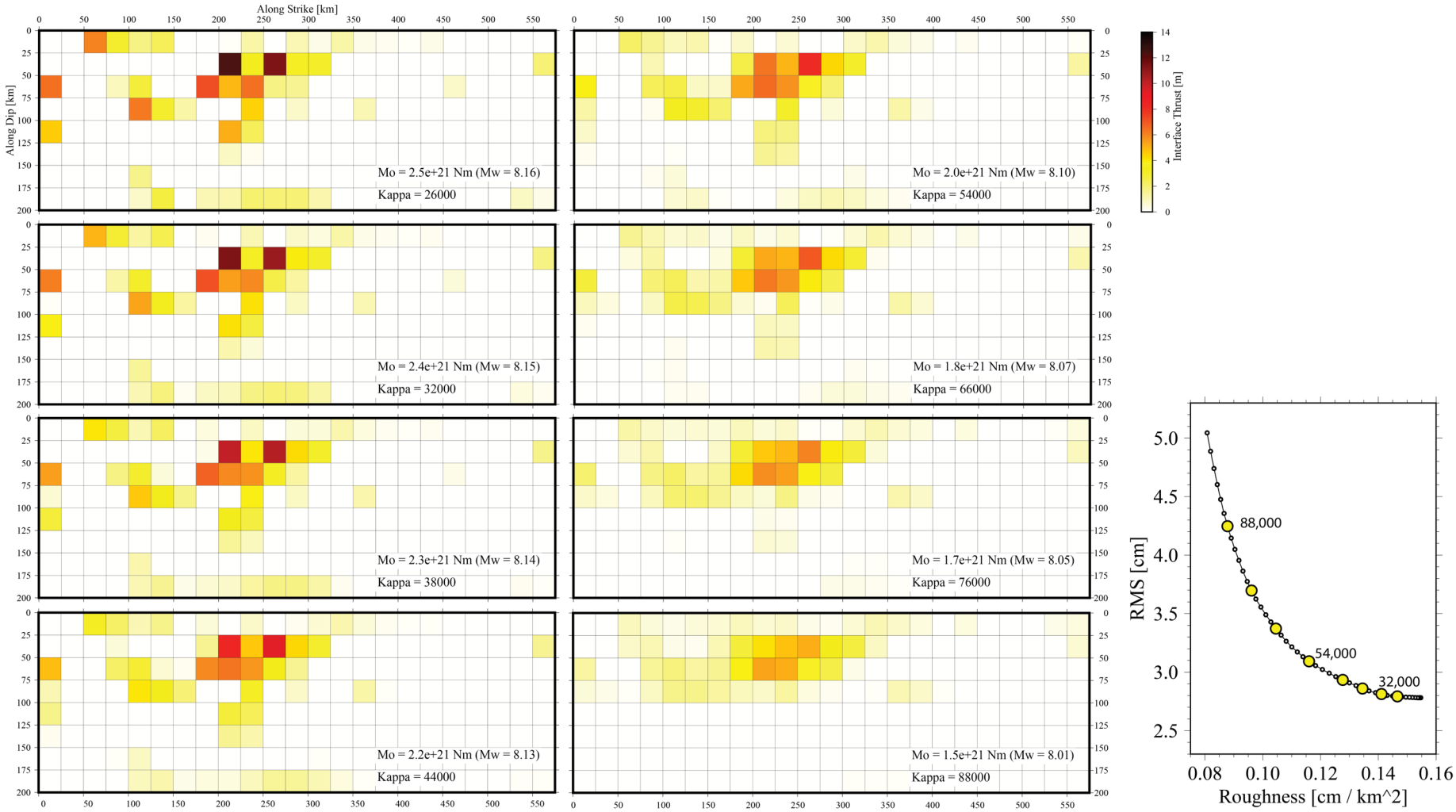

Figure S1. Variations in smoothing and misfit with an increasing kappa. The preferred solution uses a kappa of 54,000. This value was chosen to reduce the patchiness of the final solution while also sitting at the inflection between an increasing misfit and a rough solution.

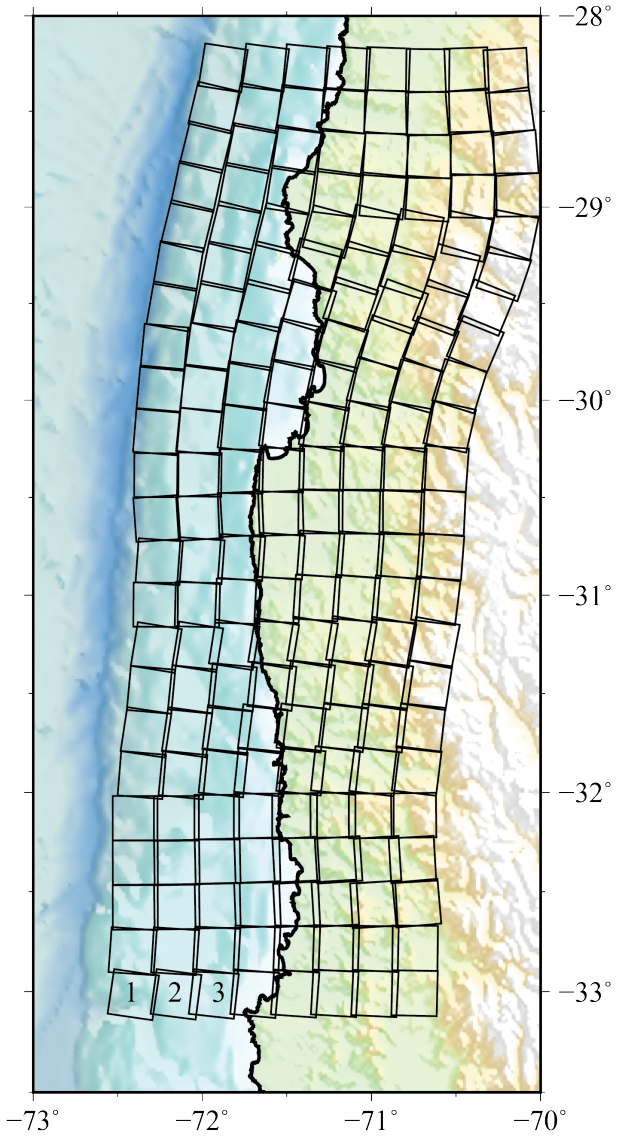

Figure S2. Subfault distribution and numbering convention. There are 184 total subfaults, 8 down dip and 23 along strike. The first subfault is labeled at the southernmost up-dip portion of the fault with increasing subfaults down dip and northward.

Table S1. Slip distribution for our preferred slip model for each discretized sub patch.

Subfault Solutions: Illapel, Chile							
	Latitude*	**Longitude***	**Depth* [km]**	**Dip**	**Strike**	**Rake**	**Slip [m]**
1	-33.015	-72.408	12.24	9.29	8.38	90	0.00
2	-33.013	-72.155	16.48	12.26	7.57	90	0.00
3	-33.011	-71.932	21.90	16.73	6.39	90	3.86
4	-33.010	-71.689	29.68	21.11	5.14	90	1.23
5	-33.010	-71.451	38.69	23.78	4.16	90	0.73
6	-33.008	-71.217	48.46	23.60	3.24	90	0.21
7	-33.009	-70.980	57.62	23.14	2.82	90	0.00
8	-33.007	-70.745	67.30	24.30	1.18	90	0.00
9	-32.798	-72.412	11.86	9.21	4.13	90	0.00
10	-32.798	-72.161	15.88	12.22	3.75	90	0.00
11	-32.792	-71.916	22.01	17.75	3.00	90	0.00
12	-32.787	-71.677	30.12	21.00	2.57	90	0.03
13	-32.785	-71.442	39.10	23.95	2.11	90	0.00
14	-32.783	-71.209	48.78	23.53	1.74	90	0.00
15	-32.785	-70.975	57.83	23.08	1.01	90	0.00
16	-32.782	-70.742	67.42	24.25	0.59	90	0.00
17	-32.577	-72.397	11.93	9.48	359.76	90	2.19
18	-32.575	-72.150	16.13	12.44	359.30	90	0.00
19	-32.570	-71.909	22.22	17.89	358.85	90	0.00
20	-32.564	-71.674	30.22	21.17	357.97	90	0.00
21	-32.561	-71.442	39.07	23.87	357.23	90	0.00
22	-32.558	-71.214	48.60	24.17	356.67	90	0.00
23	-32.564	-70.985	58.11	23.32	356.73	90	0.00
24	-32.558	-70.731	67.91	23.94	354.96	90	0.00
25	-32.354	-72.397	11.93	9.46	359.75	90	1.54
26	-32.353	-72.150	16.13	12.39	359.29	90	1.09
27	-32.347	-71.909	22.22	17.75	358.82	90	2.33
28	-32.342	-71.674	30.29	22.51	358.38	90	0.27
29	-32.342	-71.446	39.76	24.07	356.79	90	0.00
30	-32.340	-71.194	50.24	24.04	356.39	90	0.00
31	-32.339	-70.964	59.22	22.85	356.27	90	0.24
32	-32.338	-70.757	67.61	23.85	356.78	90	0.08
33	-32.131	-72.398	11.91	9.44	359.98	90	0.92
34	-32.131	-72.154	16.06	12.32	359.96	90	0.00
35	-32.125	-71.914	22.06	17.60	359.95	90	2.58

36	-32.119	-71.681	30.02	22.40	359.96	90	3.29
37	-32.118	-71.455	39.39	24.00	359.96	90	0.00
38	-32.115	-71.228	48.84	24.03	359.96	90	0.11
39	-32.119	-71.001	58.28	23.92	359.82	90	0.54
40	-32.116	-70.750	68.22	22.70	359.34	90	0.63
41	-31.913	-72.358	12.26	9.31	4.80	90	1.17
42	-31.912	-72.114	16.64	13.15	5.65	90	0.00
43	-31.902	-71.876	23.24	18.93	6.22	90	0.90
44	-31.896	-71.667	30.58	22.49	5.83	90	2.98
45	-31.892	-71.417	40.96	24.40	6.21	90	0.00
46	-31.890	-71.212	49.48	23.98	5.98	90	0.00
47	-31.895	-70.984	58.70	22.72	7.05	90	0.00
48	-31.892	-70.733	68.64	23.66	7.05	90	0.74
49	-31.697	-72.333	12.30	9.63	8.52	90	0.11
50	-31.696	-72.090	16.76	13.28	8.06	90	0.00
51	-31.685	-71.852	23.38	19.03	7.41	90	0.78
52	-31.680	-71.642	30.75	22.62	7.18	90	2.03
53	-31.675	-71.415	40.19	24.14	6.60	90	0.00
54	-31.672	-71.165	50.60	23.95	7.38	90	0.00
55	-31.675	-70.937	59.75	22.94	6.54	90	0.00
56	-31.673	-70.708	68.82	23.24	6.37	90	0.16
57	-31.481	-72.303	12.38	9.79	5.12	90	0.77
58	-31.479	-72.059	17.02	14.08	5.83	90	2.51
59	-31.469	-71.821	23.73	19.62	5.41	90	5.25
60	-31.464	-71.589	32.19	23.03	6.46	90	0.02
61	-31.456	-71.361	41.63	24.27	6.76	90	0.00
62	-31.453	-71.133	51.13	23.31	7.14	90	0.00
63	-31.459	-70.902	59.93	22.51	8.29	90	0.00
64	-31.457	-70.673	69.07	22.74	8.47	90	0.04
65	-31.266	-72.272	12.47	9.86	9.13	90	0.00
66	-31.262	-72.027	17.33	14.55	8.97	90	6.37
67	-31.253	-71.811	23.40	19.54	8.81	90	6.55
68	-31.245	-71.578	32.02	22.82	9.25	90	0.00
69	-31.238	-71.348	41.32	23.97	9.10	90	1.88
70	-31.235	-71.118	50.82	22.81	9.20	90	1.56
71	-31.240	-70.886	59.74	22.08	9.97	90	0.00
72	-31.241	-70.631	69.50	22.36	10.43	90	0.01
73	-31.049	-72.276	12.07	9.94	0.39	90	0.64
74	-31.048	-72.029	16.78	13.81	1.24	90	5.02

75	-31.031	-71.789	23.97	20.43	2.02	90	5.72
76	-31.024	-71.554	32.74	23.07	2.77	90	3.10
77	-31.014	-71.324	42.35	23.13	3.56	90	1.72
78	-31.016	-71.089	51.27	22.31	4.60	90	1.37
79	-31.021	-70.855	60.17	20.88	5.33	90	0.00
80	-31.027	-70.620	68.69	21.39	6.97	90	0.41
81	-30.829	-72.255	12.23	10.60	4.20	90	0.00
82	-30.824	-72.008	17.31	14.45	4.09	90	8.16
83	-30.807	-71.767	24.74	20.57	4.13	90	3.75
84	-30.801	-71.532	33.68	23.27	4.17	90	0.00
85	-30.790	-71.300	43.34	23.47	4.21	90	0.00
86	-30.794	-71.066	52.65	21.64	4.38	90	0.00
87	-30.796	-70.828	61.13	20.68	4.11	90	0.00
88	-30.803	-70.591	69.60	20.22	4.32	90	0.85
89	-30.609	-72.269	12.15	10.20	356.10	90	0.07
90	-30.603	-72.017	17.08	14.43	356.53	90	4.38
91	-30.585	-71.773	24.58	21.15	357.62	90	2.00
92	-30.581	-71.535	34.03	23.67	358.13	90	0.55
93	-30.572	-71.301	44.13	23.79	0.22	90	0.00
94	-30.573	-71.062	53.40	21.51	0.11	90	0.00
95	-30.576	-70.821	61.87	20.00	1.42	90	0.04
96	-30.578	-70.578	70.03	19.10	2.58	90	1.03
97	-30.386	-72.272	12.14	9.88	0.24	90	0.72
98	-30.383	-72.018	17.29	15.46	0.75	90	3.02
99	-30.367	-71.772	25.19	20.51	1.18	90	0.00
100	-30.360	-71.531	34.55	23.94	1.60	90	0.00
101	-30.352	-71.295	44.86	24.03	1.37	90	0.00
102	-30.353	-71.054	54.38	21.27	1.45	90	0.00
103	-30.356	-70.809	62.68	19.24	2.73	90	0.34
104	-30.354	-70.563	70.54	18.15	4.08	90	0.81
105	-30.163	-72.270	12.16	9.98	4.69	90	1.20
106	-30.160	-72.013	17.41	15.71	5.50	90	0.00
107	-30.144	-71.764	25.55	20.74	6.84	90	0.00
108	-30.137	-71.520	34.99	24.05	7.64	90	0.00
109	-30.134	-71.280	45.34	23.74	9.44	90	0.00
110	-30.130	-71.037	54.80	20.41	9.83	90	0.00
111	-30.137	-70.788	63.02	19.04	10.77	90	0.02
112	-30.136	-70.538	70.66	17.43	12.70	90	0.43
113	-29.943	-72.248	12.35	10.50	5.20	90	0.53

114	-29.941	-71.986	17.84	15.94	6.83	90	0.00
115	-29.927	-71.733	25.98	21.17	8.25	90	0.00
116	-29.919	-71.485	35.64	23.66	10.52	90	1.27
117	-29.920	-71.238	45.80	23.13	12.55	90	0.00
118	-29.918	-70.988	54.97	20.30	14.67	90	0.00
119	-29.928	-70.734	63.11	19.14	15.93	90	0.00
120	-29.927	-70.479	70.87	17.60	17.20	90	0.23
121	-29.727	-72.224	12.38	10.52	5.37	90	0.35
122	-29.726	-71.955	18.07	15.81	7.75	90	0.00
123	-29.718	-71.692	26.01	20.37	10.15	90	0.00
124	-29.712	-71.435	35.57	22.53	13.31	90	0.37
125	-29.718	-71.178	45.31	22.27	16.02	90	0.00
126	-29.704	-70.912	54.06	20.43	18.80	90	0.00
127	-29.713	-70.650	62.58	20.24	20.76	90	0.00
128	-29.712	-70.386	70.71	18.64	22.72	90	0.02
129	-29.516	-72.181	12.48	10.41	10.10	90	0.09
130	-29.516	-71.905	18.31	15.40	12.00	90	0.00
131	-29.512	-71.635	26.13	18.90	14.26	90	0.00
132	-29.514	-71.368	35.08	21.13	16.75	90	0.00
133	-29.505	-71.124	43.18	21.14	18.59	90	0.00
134	-29.519	-70.829	52.86	21.26	20.33	90	0.00
135	-29.522	-70.589	61.01	20.96	21.21	90	0.00
136	-29.522	-70.319	69.47	18.99	22.28	90	0.00
137	-29.306	-72.140	12.47	10.46	9.73	90	0.23
138	-29.310	-71.859	18.24	14.43	11.33	90	0.00
139	-29.314	-71.581	25.49	17.39	13.58	90	0.00
140	-29.300	-71.331	32.82	19.28	15.67	90	0.00
141	-29.315	-71.058	41.57	20.12	17.22	90	0.00
142	-29.336	-70.787	50.44	21.46	17.61	90	0.00
143	-29.331	-70.516	59.83	21.04	16.47	90	0.00
144	-29.347	-70.218	69.92	19.12	18.52	90	0.00
145	-29.099	-72.088	12.53	10.94	13.74	90	0.00
146	-29.106	-71.806	18.18	13.47	13.94	90	0.00
147	-29.115	-71.527	24.97	15.78	14.40	90	0.00
148	-29.127	-71.250	32.66	17.81	15.01	90	0.00
149	-29.122	-70.995	40.15	19.20	13.24	90	0.00
150	-29.142	-70.724	49.24	21.57	12.10	90	0.00
151	-29.152	-70.435	60.00	21.57	12.11	90	0.00
152	-29.147	-70.164	69.34	19.16	11.35	90	0.00

153	-28.893	-72.034	12.55	10.84	11.84	90	0.00
154	-28.901	-71.755	18.15	13.15	10.75	90	0.00
155	-28.912	-71.478	24.57	14.66	8.76	90	0.00
156	-28.927	-71.204	31.89	16.51	7.46	90	0.00
157	-28.943	-70.932	40.04	18.82	5.32	90	0.00
158	-28.957	-70.664	49.47	21.43	3.92	90	0.00
159	-28.943	-70.400	59.38	21.51	1.42	90	0.00
160	-28.937	-70.133	68.91	19.55	359.69	90	0.00
161	-28.688	-71.978	12.62	11.39	13.78	90	0.00
162	-28.694	-71.709	18.12	13.05	11.21	90	0.00
163	-28.703	-71.442	24.46	14.70	9.09	90	0.00
164	-28.716	-71.177	31.55	16.68	6.67	90	0.00
165	-28.728	-70.915	39.56	19.01	4.07	90	0.00
166	-28.736	-70.659	49.20	21.70	0.96	90	0.00
167	-28.720	-70.404	59.00	22.47	358.65	90	0.00
168	-28.719	-70.149	68.94	20.50	355.54	90	0.00
169	-28.481	-71.929	12.62	12.19	13.53	90	0.00
170	-28.483	-71.672	18.16	13.54	10.79	90	0.00
171	-28.487	-71.416	24.58	15.42	7.43	90	0.00
172	-28.497	-71.163	31.59	16.45	4.26	90	0.00
173	-28.505	-70.912	39.56	20.13	1.38	90	0.00
174	-28.512	-70.667	48.89	22.85	358.77	90	0.00
175	-28.501	-70.424	58.98	23.14	355.50	90	0.00
176	-28.501	-70.180	68.60	21.54	352.13	90	0.06
177	-28.273	-71.877	12.75	12.94	8.75	90	0.10
178	-28.272	-71.630	18.38	14.22	7.45	90	1.35
179	-28.272	-71.385	24.85	15.86	5.50	90	0.00
180	-28.279	-71.142	31.80	17.61	3.60	90	0.00
181	-28.281	-70.903	39.90	20.15	2.12	90	0.00
182	-28.287	-70.667	48.87	23.70	0.56	90	0.00
183	-28.281	-70.437	59.20	24.29	357.99	90	0.00
184	-28.287	-70.204	68.87	22.01	356.71	90	0.05

*Latitude, longitude, and depth are all for the center of each subfault. Each subfault has a length of 25 km and a width of 25 km.